

Unraveling the rate-determining step of C₂₊ products during electrochemical CO reduction

Received: 16 August 2023

Accepted: 16 January 2024

Published online: 30 January 2024

Check for updates

Wanyu Deng^{1,2,3}, Peng Zhang^{1,2}, Yu Qiao³, Georg Kastlunger³, Nitish Govindarajan³, Aoni Xu³, Ib Chorkendorff³, Brian Seger³✉ & Jinlong Gong^{1,2}✉

The electrochemical reduction of CO has drawn a large amount of attention due to its potential to produce sustainable fuels and chemicals by using renewable energy. However, the reaction's mechanism is not yet well understood. A major debate is whether the rate-determining step for the generation of multi-carbon products is C-C coupling or CO hydrogenation. This paper conducts an experimental analysis of the rate-determining step, exploring pH dependency, kinetic isotope effects, and the impact of CO partial pressure on multi-carbon product activity. Results reveal constant multi-carbon product activity with pH or electrolyte deuteration changes, and CO partial pressure data aligns with the theoretical formula derived from *CO-*CO coupling as the rate-determining step. These findings establish the dimerization of two *CO as the rate-determining step for multi-carbon product formation. Extending the study to commercial copper nanoparticles and oxide-derived copper catalysts shows their rate-determining step also involves *CO-*CO coupling. This investigation provides vital kinetic data and a theoretical foundation for enhancing multi-carbon product production.

Electrochemical reduction of CO (COER) into high-value fuels and chemicals is envisioned as a promising path toward storing renewable electricity in chemical bonds^{1–5}. Copper (Cu)-based catalysts are the widely accepted materials that can effectively electrochemically catalyze the formation of valuable multi-carbon (C₂₊) products with reasonable selectivity and activity^{6–8}. However, its electrochemical performance still has deficiencies that are providing barriers for its commercialization^{9–11}. An in-depth understanding of the reaction mechanism can guide the improvement of their activity and selectivity, as well as improve the energy efficiency and economics of the entire electrolyzer.

Recently, many mechanistic studies have been reported relating to reaction intermediate species^{12–16}, reaction paths^{17–20}, reaction rate-

determining steps (RDSs)^{13,21–23}, and the influence of electrolytes^{24–26}. The identification of the RDS, as the most critical mechanism guide, still lacks comprehensive and convincing experimental evidence. Three mechanisms have been generally proposed as the potential RDS through density functional theory calculation, including *CO-CO(g) coupling^{13,27}, *CO-*CO coupling^{21,22,28–30}, and the protonation of *CO to *CO(H)^{20,28,29,31,32}. Recent kinetic data has shown that the first mechanism is highly unlikely to be the RDS because the current density of C₂₊ is a constant in the CO partial pressure range of 0.6 to 1.0 bar²¹, and this mechanism would suggest it should be first order in high CO pressure. According to Li et al., the *CO-*CO coupling was favored as RDS due to a Tafel slope of 118 mV·dec⁻¹, CO reaction order (*n*_{CO}) of 0 at higher CO pressure, and pH independence of C₂₊ current density at electrolytes

¹Key Laboratory for Green Chemical Technology of Ministry of Education, School of Chemical Engineering and Technology, Tianjin University, Collaborative Innovation Center of Chemical Science and Engineering (Tianjin), Tianjin 300072, China. ²Joint School of National University of Singapore and Tianjin University, International Campus of Tianjin University, Binhai New City, Fuzhou 350207, China. ³Department of Physics, Technical University of Denmark, 2800 Kgs Lyngby, Denmark. ✉e-mail: brse@fysik.dtu.dk; jl.gong@tju.edu.cn

Table 1 | Summary of proposed reaction schemes with (*CO coupling as the possible RDS for C₂₊ products formation (detailed derivations are shown in Supplementary Note 1)

Step ^a	Proposed reaction scheme for C ₂₊ products formation	CO pressure	n _{CO}	n _{H⁺}	n _{H₂O}
A1	CO + * → *CO				
A2	*CO + *CO + e ⁻ $\xrightarrow{\text{RDS}}$ *C ₂ O ₂ ⁵⁻ + *	High	0	0	0
		Low	2	0	0
B1	CO + * → *CO				
B2	*CO + CO + e ⁻ $\xrightarrow{\text{RDS}}$ *C ₂ O ₂ ⁵⁻	High	1	0	0
		Low	2	0	0

^aA_i and B_i represents the reaction step of *i* in mechanism A and B, respectively.

with pH ranging from 7 to 13³⁰. This mechanism was further supported by the recent theoretical-experimental study by Kastlunger et al., where they found pH-independent activity in both alkaline and acidic conditions³³. However, a more detailed analysis revealed the *n*_{CO} was -1 at lower CO pressures^{31,34}. This was consistent with the RDS of *CO protonation to *CO(H), but it cannot explain the pH independence of the C₂₊ products current density in acidic conditions. Thus, a consistent and convincing RDS still needs further experimental exploration and analysis. Although previous studies have undertaken similar investigations, no convincing results have been obtained thus far. The primary reason for this is the incomplete analysis of dynamics, leading to insufficient experimental design and erroneous data analysis, among other factors, which have resulted in extensive controversies in this field^{31,34}.

In this study, the RDS of COER to C₂₊ products was investigated by combining and comprehensively analyzing theoretical derivations and kinetic experimental results. Based on various previously proposed RDSs, we first derived several possible rate expressions according to kinetics. To verify the above preliminary assumptions, the RDS was determined by adjusting the electrolyte pH, proton source, and CO partial pressure. Here, polycrystalline Cu made by sputter deposition was used as the model catalyst to investigate the RDS of COER to C₂₊ products. After analysis those data, the hypothesized reaction mechanism was verified, and the data showed that the dimerization of two adsorbed *CO was the RDS. To exclude the potential effect of morphological or electronic state of Cu catalysts, similar experiments were conducted and the mechanism was approved to be the same over those catalysts.

Results

The theoretical kinetic derivations to guide mechanism verification

Based on previous DFT calculated and experimental mechanisms^{13,21,22}, this work first assumes possible RDSs of COER to C₂₊ products. The (*CO coupling (Table 1) and *CO protonation (Table 2) mechanisms were studied. Table 1 is further broken into two divisions: *CO-*CO coupling (step A2) or a *CO-CO(aq) coupling (step B2). In Table 2, the mechanism with the *CO protonation as the RDS is classified according to the source of the protons: H₂O (step C2), H⁺ (step D2), *H from H₂O (step E3), or *H from H⁺ (steps F3). By analyzing the specific RDS, we were able to speculate on the preceding and following reaction processes, which are detailed in Tables 1, 2 (See Supplementary Note 1 for more speculating detail).

Combining the different proposed mechanisms, the theoretical current density can be calculated by using the kinetic derivation as our previous work demonstrated³⁵. The detailed derivation process can be found in the Supplementary Note 1. After obtaining the expression, theoretical parameters such as the reaction order of a specific reactant can be obtained from this expression, which can give guidance towards expected kinetic trends from experiments. Taking the RDS of

Table 2 | Summary of proposed reaction schemes with *CO protonation as the possible RDS for C₂₊ products formation (detailed derivations are shown in Supplementary Note 1)

Step ^a	Proposed reaction scheme for C ₂₊ products formation	CO pressure	n _{CO}	n _{H⁺}	n _{H₂O}
C1	CO + * → *CO				
C2	*CO + H ₂ O + e ⁻ $\xrightarrow{\text{RDS}}$ *CO(H) + OH ⁻	High	0	0	1
		Low	1	0	1
D1	CO + * → *CO				
D2	*CO + H ⁺ + e ⁻ $\xrightarrow{\text{RDS}}$ *CO(H)	High	0	1	0
		Low	1	1	0
E1	CO + * → *CO				
E2	H ₂ O + * + e ⁻ → *H + OH ⁻				
E3	*CO + *H $\xrightarrow{\text{RDS}}$ *CO(H) + *	High	-1	1	0
		Low	1	1 - -1 ^b	0
F1	CO + * → *CO				
F2	H ⁺ + * + e ⁻ → *H				
F3	*CO + *H $\xrightarrow{\text{RDS}}$ *CO(H) + *	High	-1	1	0
		Low	1	1 - -1	0

^aC_i, D_i, E_i, and F_i represent the reaction step of *i* in mechanism C, D, E and F, respectively.

^b1 - -1 represents that the value is ≥ -1 and ≤ 1 , and all the other expressions are similar.

two *CO coupling (step A2) as an example, the theoretical rate expression is derived as follows

$$j_{C2+} = k_{A2}^0 \left(\frac{K_{CO}^0 H_{CO} P_{CO} [L]}{1 + K_{CO}^0 H_{CO} P_{CO}} \right)^2 \exp(-\alpha f \eta) \quad (1)$$

Where j_{C2+} is the current density of C₂₊ products; k^0 is the standard forward rate constant and A2 in k_{A2}^0 represents the k^0 of step A2; K_{CO}^0 is the standard equilibrium constant of CO adsorption; [L] is the concentration of surface reaction sites; H_{CO} is the Henry's constant of CO gas; P_{CO} is the pressure of CO gas; α is the transfer coefficient; $f = F/RT$, where R is the ideal gas constant, T is absolute temperature, and F is the Faraday constant; η is the overpotential for the cathodic reaction. In Eq. (1), the only adsorbate of any substantial coverage is assumed to be *CO. This assumption is consistent with the low coverage of *H on the Cu surface calculated by density functional theory (see Supplementary Note 2 for simulated *H coverages). According to Eq. (1), the reaction orders of H⁺ (n_{H^+}) and H₂O (n_{H_2O}) are both 0. The n_{CO} can be calculated by

$$n_{CO} \equiv P_{CO} \frac{\partial \ln j_{C2+}}{\partial P_{CO}} \quad (2)$$

Combining Eqs. (1) and (2) yields:

$$n_{CO} = \frac{2}{K_{CO}^0 H_{CO} P_{CO} + 1} \quad (3)$$

Thus, the n_{CO} varies from 2 to 0 with increasing P_{CO} .

Similarly, the theoretical kinetic parameters corresponding to each mechanism can be deduced (Tables 1 and 2). Because different reaction mechanisms will correspond to different reaction orders, they can be later measured by experiments to verify the hypothetical mechanism and thus obtain the true RDS of COER to C₂₊ products. Although Tafel analysis is commonly used to study the RDS, it is not considered in this work. It is difficult to obtain an accurate value because it is very sensitive to mass transfer and the transfer coefficient is unknown^{36,37}.

The fabrication of Cu catalysts for COER

To elucidate the RDS of COER to C_{2+} products, polycrystalline Cu was chosen as the model catalyst. Cu was deposited on Si(100) wafers by magnetron sputtering. According to the survey X-ray photoelectron spectroscopy (XPS) spectra, no signal of the substrate materials was found on the samples indicating that the substrate was totally covered by Cu (Supplementary Fig. 3a, b). X-ray diffraction (XRD) patterns (Supplementary Fig. 3c) show that these films have polycrystalline structures. Scanning electron microscopy (SEM) images (Supplementary Fig. 3d, e) show the Cu catalyst films are evenly distributed over the substrates. The model catalysts were then used to study the RDS. Since Cu catalysts in industrial applications are generally polycrystalline rather than single crystals, this also allows the experimental results of this model catalyst to be more generalizable.

The electrochemical activity measurements were conducted in a custom three-electrode cell, where the cathodic electrolyte is continuously bubbled with CO and then injected into the cathode by a peristaltic pump. The CO transfer limitation was greatly suppressed by the high flow rate of the electrolyte with a boundary layer thickness of 12 μm in our setup (Supplementary Fig. 4), which was beneficial for the following electrochemical kinetics study. For COER performance, C_2H_4 , CH_4 , C_2H_6 , and H_2 were the main gas products; glycolaldehyde, acetate, ethylene glycol, ethanol, propionaldehyde, and n-propanol were the main liquid products. The total Faradaic efficiency is near 100% (with variation within 10%) in seven different electrolytes (Supplementary Fig. 5). The CH_4 , C_2H_4 , and H_2 current densities are consistent throughout one-hour tests (Supplementary Fig. 6), indicating the Cu catalyst is sufficiently stable for analyzing the RDS.

pH dependency experiments to determine n_{H^+}

To ascertain the n_{H^+} , four electrolytes with varied pH were used. These electrolytes are 0.1 M KOH (pH 13), 0.1 M $KHCO_3$ (pH 9), 0.1 M KH_2PO_4 (pH 3, prepared by adding H_3PO_4 to KOH solution), and 0.05 M K_2SO_4

(pH 2, prepared by adding H_2SO_4 to KOH solution). By applying the same cation concentration for all electrolytes, concerns about the effects of the cation are eliminated^{38–40}. However, it is challenging to rule out the impact of anions in this situation. Adjusting the pH of electrolytes with the same level of K^+ ions cannot prevent the change of electrolyte anions. Out of these four anions, $H_2PO_4^-$ is strongly adsorbed over Cu and may also act as a proton source^{41,42}, which would bias the experimental results under acidic conditions. To avoid this, an acidic solution of weakly adsorbed and proton-free SO_4^{2-} anion⁴³ was also chosen as a test electrolyte.

As shown in Fig. 1a, the current density of the C_{2+} products remain relatively constant with decreasing pH at the same potential. This phenomenon is also observed for the specific C_{2+} products: C_2H_4 (Fig. 1b), ethanol (Supplementary Fig. 7a), n-propanol (Supplementary Fig. 7b), and acetate (Supplementary Fig. 7c). These results indicate that the increase in proton concentration does not promote the formation of C_{2+} products, thus the n_{H^+} should be 0 or even negative.

On the contrary, the activity of the COER to CH_4 and hydrogen evolution reaction (HER) is enhanced as the pH decreases (Fig. 1c, d), which is consistent with the results from the literature^{30,44,45}. More analysis can be found below Supplementary Fig. 7. Considering that protons are continuously consumed under COER (as well as the competing hydrogen evolution reaction, HER), the local pH will increase. By constructing a mass transfer model, it was discovered that while there is a slight variation in local pH in comparison to bulk pH, the trend of pH remains the same (Supplementary Fig. 8 and Supplementary Note 3). Therefore, the local pH shift does not affect the experiment's conclusion.

KIE experiments to determine whether H_2O is engaged in the RDS or its previous steps

It is important to acknowledge that in an aqueous system, H_2O is commonly present at a substantial concentration as an electrolyte, and

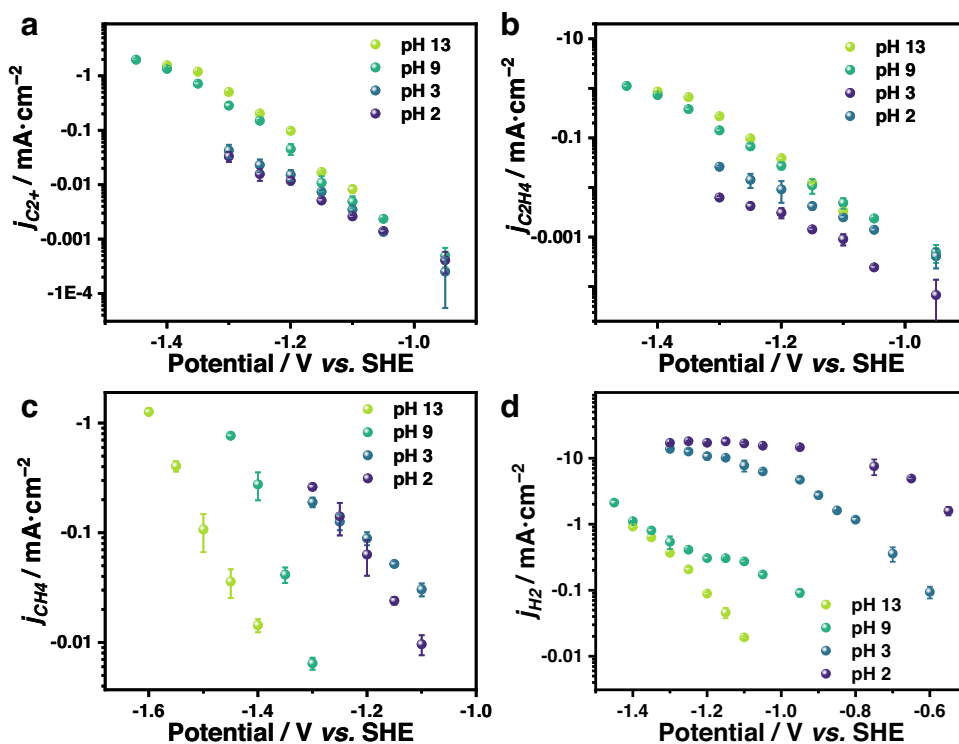


Fig. 1 | The pH dependency for COER. The current density of C_{2+} (a), C_2H_4 (b), CH_4 (c), and H_2 (d) versus potential in CO-saturated electrolytes with different pH. All are measured in a potential range where the current is not too large in order to

avoid getting into the limiting mass transport regime of CO. Error bars are means \pm standard deviation ($n = 3$ replicates).

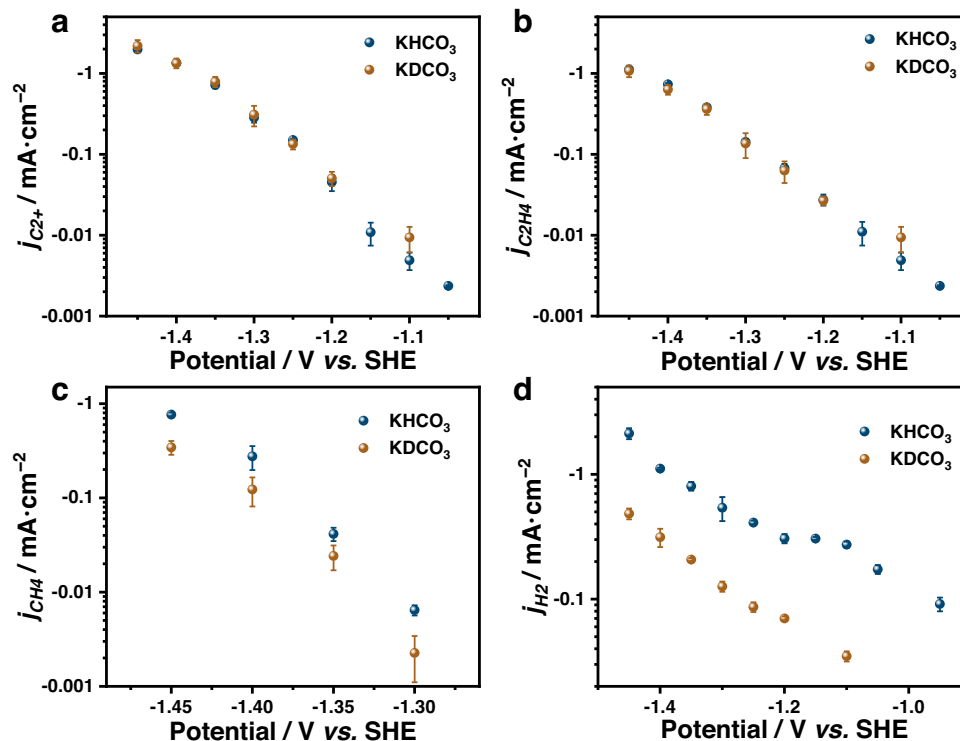


Fig. 2 | Kinetic isotope effect for COER. The current density of C_{2+} (a), C_2H_4 (b), CH_4 (c), and H_2 (d) versus potential in CO-saturated 0.1 M $KHCO_3$ and $KDCO_3$ electrolytes. Error bars are means \pm standard deviation ($n = 3$ replicates).

its concentration remains constant throughout the reaction. Consequently, altering the H_2O concentration does not enable us to determine its direct involvement in the reaction. However, the use of hydrogen/deuterium kinetic isotope exchange (H/D KIE) experiments can provide a means to differentiate whether H_2O is engaged in the RDS of the reaction. The KIE experiments of COER in D_2O ($KDCO_3$) and H_2O ($KHCO_3$) solutions were conducted. From Fig. 2a, b, the current densities of C_{2+} and C_2H_4 are identical under the two tested conditions, revealing that H_2O is not involved either in the RDS or before the RDS. Supplementary Fig. 9 further illustrates the KIE effect for specific C_{2+} products, including ethanol, n-propanol, and acetate. These results show that deuterium atoms can slightly increase ethanol generation while decreasing acetate production.

The current densities of CH_4 and H_2 were used as a benchmark of the KIE experiments. With the addition of deuterium atoms, the current densities of both CH_4 and H_2 dropped (Fig. 2c, d) in agreement with the fact that protons are involved in the RDS as reported in the literature^{30,44,45}. The detailed explanations of the KIE can be found below Supplementary Fig. 10. Similarly, the KIE was tested in H_2O and D_2O solutions of KOH (pH 13) and KH_2PO_4 (pH 3) to exclude the potential effect of pH (Supplementary Fig. 10 and 11), where the same conclusion can be drawn. The previous literature reported that KIEs of H/D over various different copper surface can vary from 2 to 1^{16} . It is conceivable that the surface state of the catalyst may be a determining factor in altering the RDS. The mechanistic system research method proposed in this work is expected to effectively guide future explorations of RDS in other Cu-based catalyst reactions.

CO partial pressure effects to determine n_{CO}

The partial pressure of CO (0.02 to 1 bar) was adjusted by changing the ratio of CO to Ar gas. All the experiments were conducted in a KOH electrolyte at -1.3 V vs. SHE. Prior to conducting the reaction kinetics analysis, the conversion rate of CO under different partial pressures was calculated to be approximately 0.02% (Supplementary Fig. 12).

This confirms that there will be sufficient CO supply at low pressures. Figure 3a shows that the activity of C_{2+} products rises along with the CO partial pressure until it reaches 0.5 bar, after which the partial current density becomes constant. By using a simple linear fitting method, the n_{CO} is roughly equivalent to 1 at partial pressures lower than 0.15 bar and 0 at partial pressures higher than 0.5 bar, which are consistent with data reported in the literature^{21,30,31}. However, a simple interval linear fit, without the possibility of extrapolation, is likely to lead to erroneous conclusions that n_{CO} is between 1 - 0 from low to high CO pressure.

In order to be more accurate, the theoretical rate expression is employed as the fitting formula (see Supplementary Note 4 for more fitting detail). It was determined that only the mechanism of step A2 (*CO-*CO coupling as the RDS) can fit the experimental data well (Fig. 3 and Supplementary Fig. 13–16). To exclude the influence of pH, similar CO partial pressure experiments were measured in KOH electrolyte under alkaline condition at -1.3 V vs. SHE. The same conclusion can be obtained (Supplementary Fig. 17).

When discussing n_{CO} , there are one thing to keep in mind. The data must first be fitted according to the theoretical rate expression; otherwise, it may result in incorrect conclusions due to the lack of suitable low or high CO pressure data. For example, n_{CO} is assumed to be between 1 and 0 by a simple interval linear fit, but after the non-linear fitting, only step A2 is found to be consistent with the experimental data.

Discussion

The mechanisms in Tables 1, 2 were subsequently verified by the previous experimental results, which confirmed the reaction orders of CO and H^+ are 0 and ≤ 0 , respectively at a CO pressure of 1 bar. Moreover, H_2O does not participate in the RDS or any preceding steps at a CO pressure of 1 bar. Out of the above-mentioned hypothesized processes, only the mechanism of *CO-*CO coupling (step A2) as the RDS satisfies the experimental findings at the same time.

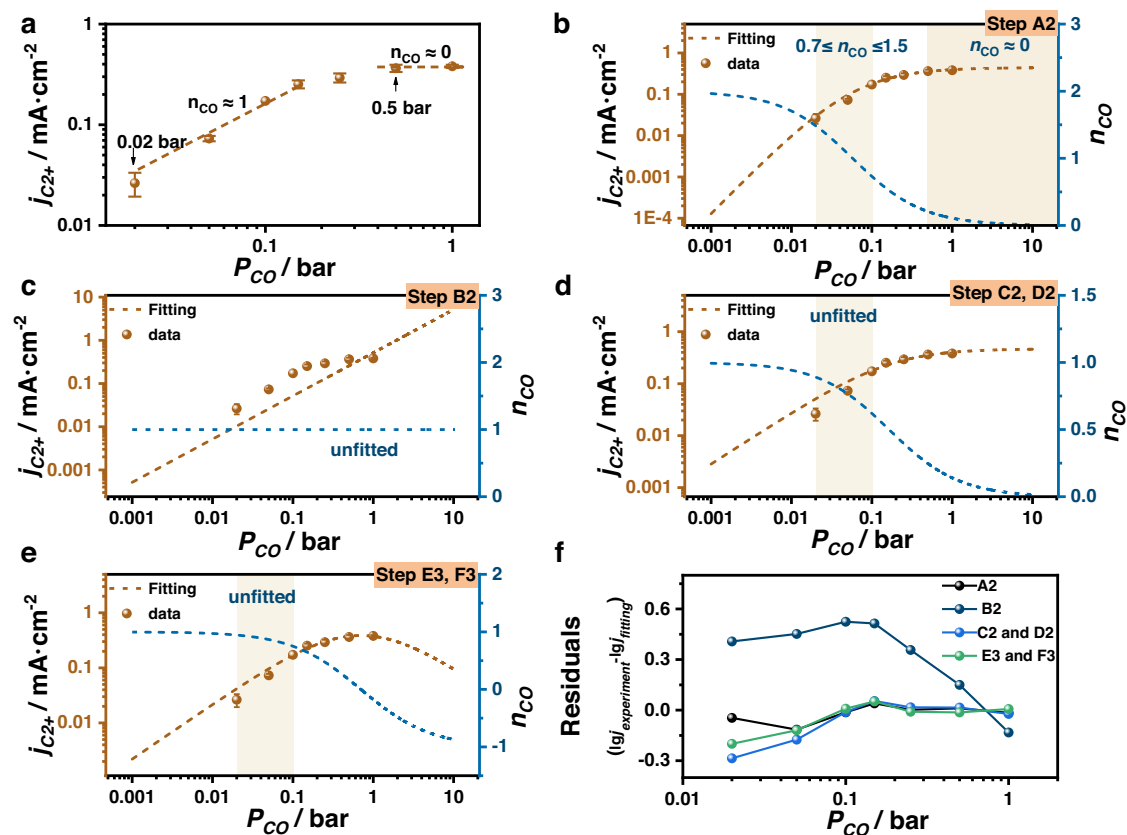


Fig. 3 | CO reaction order for COER. The current density of C_{2+} products versus CO partial pressure for interval linear (a) and non-linear (b–e) data fitting as well as their residuals (f). The equations used for fitting (b–e) are the theoretical rate expressions corresponding to different mechanisms (see Supplementary Table 1

for all the fitting parameters). All those data are collected in CO-saturated 0.1M KOH electrolyte at -1.3 V vs. SHE. Error bars are means \pm standard deviation ($n = 3$ replicates).

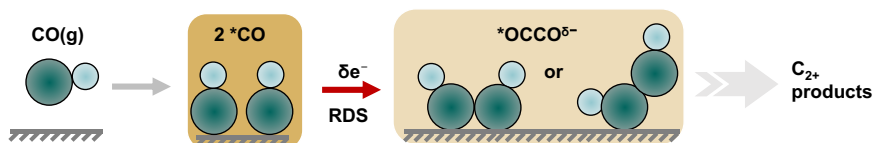


Fig. 4 | Reaction mechanism of C_{2+} products diagram for COER on polycrystalline Cu. The CO first adsorbs over Cu catalysts, following two adsorbed CO coupling as the RDS of C_{2+} products.

To further demonstrate the generalizability of the conclusions, the investigations in other Cu-based catalytic reactions, commercial Cu nanoparticles (Cu NP 40–60 nm) and oxide-derived Cu (OD-Cu), was carried out. It can also be observed that the activity of C_{2+} products does not increase with higher H^+ concentration (Supplementary Fig. 18–21). The KIE was approximately equal to 1, and the partial pressure experiment of CO could only be fully fitted using the theoretical formula for Step 2 ($^*CO\text{-}^*CO$ coupling). Thus, for both commercial Cu and OD-Cu, the RDS for C_{2+} products should also be the $^*CO\text{-}^*CO$ coupling.

It is worth mentioning that our primary experiments were conducted under both acidic and alkaline conditions. Therefore, our conclusions should not vary with pH. However, the activity of ethanol, acetate, and n-propanol products was observed to be very low. As a result, the experimental data primarily reflected the contribution of C_2H_4 . Therefore, the conclusions drawn from this data are more applicable to C_2H_4 , and it cannot be ruled out that specific C_{2+} products may have different RDS than those mentioned in the article. In the future, the research of a particular product or C_{3+} products should

be conducted. To investigate this, it would be necessary to identify a catalyst that favors the production of this product and then employ similar kinetic analysis methods as used in this work. By considering various possibilities, designing experiments, and finally validating hypotheses, it would be possible to unravel the RDS for specific C_{2+} products formation.

In conclusion, this work combines theoretical derivation with hypothesized mechanisms to design a method that can effectively verify the mechanism of the RDS of COER to C_{2+} products. It provides comprehensive kinetic data through experiments, including pH dependency, KIE, and CO partial pressure experiments. Specifically, the reaction is not accelerated by an increase in proton concentration, it is not slowed down by the replacement of deuterium atoms for H^+ , and the C_{2+} reactivity rises initially before remaining constant as CO partial pressure increases. Verifying these hypothetical reaction mechanisms according to the experiment data, it was found that only the dimerization of two adsorbed *CO is the most likely RDS (Fig. 4). This finding suggests that promoting the C-C coupling is key to enhancing C_{2+} products.

Methods

Electrode preparation

Cu thin films were deposited onto single-crystal Si wafers with the (100) orientation using an AJA ATC Orion-5 magnetron sputtering system. To enhance the adhesion between the catalysts and the Si wafers, Ti films with a thickness of approximately 15 nm were first deposited on the Si wafers⁴⁷. In detail, the Si wafers were etched with Ar⁺ ions for 5 min with a power of 40 W to clean the silicon oxide on Si wafers. Then, 15 nm Ti films (99.9999%) were deposited as binders between catalysts and Si wafers at the power of 100 W. Cu catalyst films (99.9999%) with a thickness of 100 nm were deposited over Ti at 130 W. For commercial Cu nanoparticle was purchase from Sigma-Aldrich with 40 - 60 nm size. OD-Cu is prepared by subjecting commercial Cu nanoparticles to a reduction process under in-situ negative potential after being treated in an O₂ atmosphere at 300 °C for 1 hour.

Electrode characterization

The crystal structures of the Cu thin films were analyzed with a Rigaku Smartlab X-ray diffractometer (XRD) using Cu K α radiation (40 kV, 40 mA). The near-surface compositions of the thin films were measured with a Kratos Axis Ultra DLD X-ray photoelectron spectrometer (XPS). All spectra were acquired using monochromatized Al K α radiation (15 kV, 15 mA). The kinetic energy scale of the measured spectra was calibrated by setting the C 1s binding energy to 284.8 eV. The surface structure of those thin films was recorded using an FEI XL30 Sirion scanning electron microscope (SEM) at the acceleration voltage of 5 kV, ET-detector, SE mode.

Chemicals

Potassium hydroxide hydrate (KOH·H₂O, Merck, 99.995%), potassium carbonate (K₂CO₃, Merck, 99.995%), phosphoric acid (H₃PO₄, Sigma Aldrich, 85 wt% in H₂O, 99.99%), sulfuric acid (H₂SO₄, Sigma Aldrich, 99.999%), deuterium oxide (D₂O, Sigma Aldrich, 99.9 atom % D).

Preparing electrolyte

Seven different electrolytes were used in the work, including 0.1 M KOH (pH 13), 0.1 M KHCO₃ (pH 9, the electrolyte was made by bubbling CO₂ into 0.05 M K₂CO₃ electrolyte for 4 hours and then bubbling Ar overnight to get rid of excess CO₂), 0.1 M KH₂PO₄ (pH 3, the electrolyte was made by neutralizing KOH with H₃PO₄ to pH 3, and the K⁺ concentration in the electrolyte was kept at 0.1 M), 0.05 M K₂SO₄ with H₂SO₄ (pH 2, the electrolyte was made by neutralizing KOH with H₂SO₄ to pH 2, and the K⁺ concentration in the electrolyte was kept at 0.1 M), 0.1 M KOH in D₂O, 0.1 M KDCO₃ (the electrolyte was made by the same method as 0.1 M KHCO₃ except the H₂O was changed to D₂O), and 0.1 M KH₂PO₄ in D₂O (the electrolyte was made by the same method as 0.1 M KH₂PO₄ except the H₂O was changed to D₂O). All the solutions were prepared using 18.2 milli-Q water (Synergy UV) or deuterium oxide (D₂O, Sigma Aldrich, 99.9 atom % D).

Electrochemical characterization

Most electrochemical activity measurements were conducted in a custom electrochemical cell machined from PEEK at room temperature and atmospheric pressure (Supplementary Fig. 4a). The cell was sonicated in 20 wt% nitric acid and thoroughly rinsed with milli-Q water before all experimentation. The working and counter electrodes were parallel and separated by a bipolar membrane (BPM, Fumasep FBM). The exposed geometric surface area of each electrode was 1 cm². The electrolyte volumes in the cathodic and anodic chambers were 7 mL and 0.9 mL, respectively. The counter electrode was iridium dioxide (IrO₂) purchased from Dioxide Materials. The working electrode potential was referenced against a Hg/HgO electrode in 0.1 M KOH (ALVATEK, RE-61AP) that was calibrated against a homemade standard hydrogen electrode (SHE). The solutions mentioned before were used as the cathodic electrolyte. 0.1 M KHCO₃ was used as the

anodic electrolyte. The cathodic electrolyte was sparged with CO (99.999% Praxair Inc.) or mixture with Ar (99.999% Praxair Inc.) at a certain rate, where the 10 sccm of CO was used for pH-dependence and KIE experiments, and 20 sccm of different ratio of CO and Ar was used for partial pressure experiments. Note that CO gas must be purified by using a carbonyl trap (LPM Carbonyl Trap) in order to eliminate metal ions as Ni, Fe, etc. from metal tubes. Then gas-saturated electrolyte was pumped into the cathodic chamber by using a peristaltic pump (SHENCHEN LabN6) with the rate of 100 rev/min. Here, the experiment process in this pump speed cannot be significantly diffusion-limited, since we have obtained relatively straight Tafel slopes over 3 orders of magnitude in the current (Figs. 1, 2).

For the flow cell experiments, they were performed in three-component cell configuration. For specific flow cell details, please refer to our previous the article⁴⁸. A constant CO flowrate of 30 mL·min⁻¹ was purged into gas compartment, and 30 mL catholyte and anolyte were applied, respectively. A part of CO diffused to the catalyst surface in electrolyte for CO conversion, forming various gaseous and liquid products. The gaseous products mixed with unreacted CO were vented out of the electrolyzer, injecting into the gas-sampling loop of a gas chromatography for identification and quantification. The liquid products were measured from both catholyte and anolyte.

The produced CO and H₂ are tested by gas chromatography (GC, Thermo scientific, TRACE 1300). Ar was used as the carrier gas. The GC was equipped with a packed Molsieve 5 A column, a packed Hayesep Q column, and an Rt-Qbond column to separate the gaseous products. Thus, H₂ and carbon-containing products (CH₄, C₂H₄, C₂H₆) could be identified using a thermal conductivity detector and a flame ionization detector, respectively. The liquid-phase products are analyzed after the electrolysis using high-performance liquid chromatography (HPLC, Agilent 1200 series). Liquid-phase products were separated by an Aminex HPX-87H column (Bio-Rad) that was maintained at 50 °C. The HPLC was equipped with a refractive index detector (RID). 5 mM H₂SO₄ solution was used as the carrier liquid with 0.3 mL min⁻¹ speed. Some raw HPLC sample data were shown in Supplementary Fig. 22. The response signals of the RID were calibrated by solutions with different concentrations (Supplementary Fig. 23).

Electrochemical characterizations were performed using a Biologic VSP-300 potentiostat. All electrochemical measurements were recorded versus the reference electrode and converted to the SHE scales. IR compensation (ZIR) was used to determine the uncompensated resistance (R_u) of the electrochemical cell.

The Cu catalyst was firstly reduced by conducting chronoamperometry at -0.9 V vs. SHE for 10 min. Under this potential, no carbon-related products can be produced. The electrocatalytic activity of the Cu catalyst was assessed by conducting chronoamperometry at different potentials for 1 hour. The gas product was measured every 10 min, and the liquid product was measured after one-hour experiments. Each data was tested at least three separate times to ensure the statistical relevance of the observed trends.

Data availability

All the data that support the findings of this study are available within the paper and its Supplementary Information files, or from the corresponding author on reasonable request.

References

1. Nitopi, S. et al. Progress and perspectives of electrochemical CO₂ reduction on copper in aqueous electrolyte. *Chem. Rev.* **119**, 7610–7672 (2019).
2. Garg, S., Giron Rodriguez, C. A., Rufford, T. E., Varcoe, J. R. & Seger, B. How membrane characteristics influence the performance of CO₂ and CO electrolysis. *Energy Environ. Sci.* **15**, 4440–4469 (2022).

3. Birdja, Y. Y. et al. Advances and challenges in understanding the electrocatalytic conversion of carbon dioxide to fuels. *Nat. Energy* **4**, 732–745 (2019).
4. Grim, R. G. et al. Transforming the carbon economy: challenges and opportunities in the convergence of low-cost electricity and reductive CO₂ utilization. *Energy Environ. Sci.* **13**, 472–494 (2020).
5. Stephens, I. E. L. et al. 2022 roadmap on low temperature electrochemical CO₂ reduction. *J. Phys. Energy* **4**, 042003 (2022).
6. Zhang, H. C., Li, J., Cheng, M. J. & Lu, Q. CO electroreduction: current development and understanding of Cu-based catalysts. *ACS Catal.* **9**, 49–65 (2019).
7. Fan, Q. et al. Electrochemical CO₂ reduction to C₂₊ species: heterogeneous electrocatalysts, reaction pathways, and optimization strategies. *Mater. Today Energy* **10**, 280–301 (2018).
8. Zhu, D. D., Liu, J. L. & Qiao, S. Z. Recent advances in inorganic heterogeneous electrocatalysts for reduction of carbon dioxide. *Adv. Mater.* **28**, 3423–3452 (2016).
9. Bushuyev, O. S. et al. What should we make with CO₂ and how can we make it? *Joule* **2**, 825–832 (2018).
10. Jouny, M., Luc, W. & Jiao, F. General techno-economic analysis of CO₂ electrolysis systems. *Ind. Eng. Chem. Res.* **57**, 2165–2177 (2018).
11. Shin, H., Hansen, K. U. & Jiao, F. Techno-economic assessment of low-temperature carbon dioxide electrolysis. *Nat. Sustain.* **4**, 911–919 (2021).
12. Schouten, K. J. P., Kwon, Y., van der Ham, C. J. M., Qin, Z. & Koper, M. T. M. A new mechanism for the selectivity to C₁ and C₂ species in the electrochemical reduction of carbon dioxide on copper electrodes. *Chem. Sci.* **2**, 1902–1909 (2011).
13. Calle-Vallejo, F. & Koper, M. T. M. Theoretical considerations on the electroreduction of CO to C₂ species on Cu(100) electrodes. *Angew. Chem. Int. Ed.* **52**, 7282–7285 (2013).
14. Clark, E. L. et al. Explaining the incorporation of oxygen derived from solvent water into the oxygenated products of CO reduction over Cu. *J. Am. Chem. Soc.* **141**, 4191–4193 (2019).
15. Charnay, B. P., Cui, Z., Marx, M. A., Palazzo, J. & Co, A. C. Insights into the CO₂ reduction pathway through the electrolysis of aldehydes on copper. *ACS Catal.* **11**, 3867–3876 (2021).
16. Löffler, M., Khanipour, P., Kulyk, N., Mayrhofer, K. J. J. & Katsounaros, I. Insights into liquid product formation during carbon dioxide reduction on copper and oxide-derived copper from quantitative real-time measurements. *ACS Catal.* **10**, 6735–6740 (2020).
17. Lum, Y. W., Cheng, T., Goddard, W. A. & Ager, J. W. Electrochemical CO reduction builds solvent water into oxygenate products. *J. Am. Chem. Soc.* **140**, 9337–9340 (2018).
18. Jouny, M., Luc, W. & Jiao, F. High-rate electroreduction of carbon monoxide to multi-carbon products. *Nat. Catal.* **1**, 748–755 (2018).
19. Luc, W. et al. Two-dimensional copper nanosheets for electrochemical reduction of carbon monoxide to acetate. *Nat. Catal.* **2**, 423–430 (2019).
20. Cheng, T., Xiao, H. & Goddard, W. A. Full atomistic reaction mechanism with kinetics for CO reduction on Cu(100) from ab initio molecular dynamics free-energy calculations at 298 K. *Proc. Natl. Acad. Sci. USA.* **114**, 1795–1800 (2017).
21. Li, J. et al. Effectively increased efficiency for electroreduction of carbon monoxide using supported polycrystalline copper powder electrocatalysts. *ACS Catal.* **9**, 4709–4718 (2019).
22. Schreier, M., Yoon, Y., Jackson, M. N. & Surendranath, Y. Competition between H and CO for active sites governs copper-mediated electrosynthesis of hydrocarbon fuels. *Angew. Chem. Int. Ed.* **57**, 10221–10225 (2018).
23. Zhao, Q., Martinez, J. M. P., Carter, E. A. & Charting, C. –C coupling pathways in electrochemical CO₂ reduction on Cu (111) using embedded correlated wavefunction theory. *Proc. Natl. Acad. Sci. USA.* **119**, e2202931119 (2022).
24. Ludwig, T. et al. Solvent-adsorbate interactions and adsorbate-specific solvent structure in carbon dioxide reduction on a stepped Cu surface. *J. Phys. Chem. C* **123**, 5999–6009 (2019).
25. Singh, M. R., Kwon, Y., Lum, Y., Ager, J. W. & Bell, A. T. Hydrolysis of electrolyte cations enhances the electrochemical reduction of CO₂ over Ag and Cu. *J. Am. Chem. Soc.* **138**, 13006–13012 (2016).
26. Resasco, J. et al. Promoter effects of alkali metal cations on the electrochemical reduction of carbon dioxide. *J. Am. Chem. Soc.* **139**, 11277–11287 (2017).
27. Montoya, J. H., Peterson, A. A. & Nørskov, J. K. Insights into C-C coupling in CO₂ electroreduction on copper electrodes. *ChemCatChem* **5**, 737–742 (2013).
28. Goodpaster, J. D., Bell, A. T. & Head-Gordon, M. Identification of possible pathways for C-C bond formation during electrochemical reduction of CO₂: new theoretical insights from an improved electrochemical model. *J. Phys. Chem. Lett.* **7**, 1471–1477 (2016).
29. Xiao, H., Cheng, T., Goddard, W. A. & Sundararaman, R. Mechanistic explanation of the pH dependence and onset potentials for hydrocarbon products from electrochemical reduction of CO on Cu (111). *J. Am. Chem. Soc.* **138**, 483–486 (2016).
30. Li, J. et al. Electrokinetic and in situ spectroscopic investigations of CO electrochemical reduction on copper. *Nat. Commun.* **12**, 3264 (2021).
31. Chang, X. et al. C-C coupling is unlikely to be the rate-determining step in the formation of C₂₊ products in the copper-catalyzed electrochemical reduction of CO. *Angew. Chem. Int. Ed.* **61**, e20211167 (2021).
32. Garza, A. J., Bell, A. T. & Head-Gordon, M. Mechanism of CO₂ reduction at copper surfaces: pathways to C₂ products. *ACS Catal.* **8**, 1490–1499 (2018).
33. Kastlunger, G. et al. Using pH dependence to understand mechanisms in electrochemical CO reduction. *ACS Catal.* **12**, 4344–4357 (2022).
34. Hou, J. et al. coverage and CO electroreduction on Cu via high-pressure in situ spectroscopic and reactivity investigations. *J. Am. Chem. Soc.* **144**, 22202–22211 (2022).
35. Deng, W., Zhang, P., Seger, B. & Gong, J. Unraveling the rate-limiting step of two-electron transfer electrochemical reduction of carbon dioxide. *Nat. Commun.* **13**, 803 (2022).
36. Limaye, A. M., Zeng, J. S., Willard, A. P. & Manthiram, K. Bayesian data analysis reveals no preference for cardinal Tafel slopes in CO₂ reduction electrocatalysis. *Nat. Commun.* **12**, 703 (2021).
37. Dunwell, M., Luc, W., Yan, Y. S., Jiao, F. & Xu, B. J. Understanding surface-mediated electrochemical reactions: CO₂ reduction and beyond. *ACS Catal.* **8**, 8121–8129 (2018).
38. Li, J. et al. Hydroxide is not a promoter of C₂₊ product formation in electrochemical reduction of CO on copper. *Angew. Chem. Int. Ed.* **59**, 4464–4469 (2019).
39. Ringe, S. et al. Understanding cation effects in electrochemical CO₂ reduction. *Energy Environ. Sci.* **12**, 3001–3014 (2019).
40. Ren, W., Xu, A., Chan, K. & Hu, X. A cation concentration gradient approach to tune the selectivity and activity of CO₂ electroreduction. *Angew. Chem. Int. Ed.* **61**, e202214173 (2022).
41. Niaura, G., Gaigalas, A. K. & Vilker, V. L. Surface-enhanced Raman spectroscopy of phosphate anions: adsorption on silver, gold, and copper electrodes. *J. Phys. Chem. B* **101**, 9250–9262 (1997).
42. Hochfilzer, D. et al. Transients in electrochemical CO reduction explained by mass transport of buffers. *ACS Catal.* **12**, 5155–5161 (2022).
43. Ovalle, V. J. & Waegele, M. M. Impact of electrolyte anions on the adsorption of CO on Cu electrodes. *J. Mater. Chem. C* **124**, 14713–14721 (2020).
44. Strmcnik, D. et al. Improving the hydrogen oxidation reaction rate by promotion of hydroxyl adsorption. *Nat. Chem.* **5**, 300–306 (2013).

45. Goyal, A. & Koper, M. T. M. The interrelated effect of cations and electrolyte pH on the hydrogen evolution reaction on gold electrodes in alkaline media. *Angew. Chem. Int. Ed.* **60**, 13452–13462 (2021).
46. Ma, W. et al. Electrocatalytic reduction of CO₂ to ethylene and ethanol through hydrogen-assisted C–C coupling over fluorine-modified copper. *Nat. Catal.* **3**, 478–487 (2020).
47. Todeschini, M., Bastos da Silva Fanta, A., Jensen, F., Wagner, J. B. & Han, A. Influence of Ti and Cr adhesion layers on ultrathin Au films. *ACS Appl. Mater. Interfaces* **9**, 37374–37385 (2017).
48. Hendrik, H. H. et al. Mechanism for acetate formation in electrochemical CO₂ reduction on Cu: Selectivity with potential, pH, and nanostructuring. *Energy Environ. Sci.* **15**, 3978–3990 (2022).

Acknowledgements

This work was supported by the National Key R&D Program of China (2021YFA1501503), the National Natural Science Foundation of China (22121004, 22038009, 22108197, 22250008), the Haihe Laboratory of Sustainable Chemical Transformations (CYZC202107), the Program of Introducing Talents of Discipline to Universities (No. BPO618007), the Xplorer Prize, the European Union's Horizon 2020 research, innovation program under grant agreement No. 851441 (project SelectCO₂), Villum Center for the Science of Sustainable Fuels and Chemicals (V-Sustain No. 9455).

Author contributions

W.Y.D. designed and performed the experiments. Y.Q. is responsible for collecting XPS and XRD data. G.K. and N.G. are responsible for the calculation of the H coverage. A.N.X helped the calculation of local pH. P.Z., B.S., I.C. and J.L.G. coordinated and supervised the research. All authors contributed to the writing of the manuscript.

Competing interests

The authors declare no competing interests.

Additional information

Supplementary information The online version contains supplementary material available at <https://doi.org/10.1038/s41467-024-45230-1>.

Correspondence and requests for materials should be addressed to Brian Seger or Jinlong Gong.

Peer review information *Nature Communications* thanks the anonymous reviewers for their contribution to the peer review of this work. A peer review file is available.

Reprints and permissions information is available at <http://www.nature.com/reprints>

Publisher's note Springer Nature remains neutral with regard to jurisdictional claims in published maps and institutional affiliations.

Open Access This article is licensed under a Creative Commons Attribution 4.0 International License, which permits use, sharing, adaptation, distribution and reproduction in any medium or format, as long as you give appropriate credit to the original author(s) and the source, provide a link to the Creative Commons license, and indicate if changes were made. The images or other third party material in this article are included in the article's Creative Commons license, unless indicated otherwise in a credit line to the material. If material is not included in the article's Creative Commons license and your intended use is not permitted by statutory regulation or exceeds the permitted use, you will need to obtain permission directly from the copyright holder. To view a copy of this license, visit <http://creativecommons.org/licenses/by/4.0/>.

© The Author(s) 2024